

Robust Discontinuity Indicators for High-Order Reconstruction of Piecewise Smooth Functions

Yipeng Li^a, Qiao Chen^a, Xiangmin Jiao^{a,*}

^a*Dept. of Applied Math. & Stat. and Institute for Advanced Computational Science, Stony Brook University, Stony Brook, NY 11794, USA.*

Abstract

In many applications, piecewise continuous functions are commonly interpolated over meshes. However, accurate high-order manipulations of such functions can be challenging due to potential spurious oscillations known as the Gibbs phenomena. To address this challenge, we propose a novel approach, *Robust Discontinuity Indicators (RDI)*, which can efficiently and reliably detect both C^0 and C^1 discontinuities for node-based and cell-averaged values. We present a detailed analysis focusing on its derivation and the dual-thresholding strategy. A key advantage of RDI is its ability to handle potential inaccuracies associated with detecting discontinuities on non-uniform meshes, thanks to its innovative discontinuity indicators. We also extend the applicability of RDI to handle general surfaces with boundaries, features, and ridge points, thereby enhancing its versatility and usefulness in various scenarios. To demonstrate the robustness of RDI, we conduct a series of experiments on non-uniform meshes and general surfaces, and compare its performance with some alternative methods. By addressing the challenges posed by the Gibbs phenomena and providing reliable detection of discontinuities, RDI opens up possibilities for improved approximation and analysis of piecewise continuous functions, such as in data remap.

Keywords: piecewise continuous functions, interpolation, approximation, discontinuity detection, high-order reconstruction, data remapping

*Corresponding author

Email address: xiangmin.jiao@stonybrook.edu (Xiangmin Jiao)

1. Introduction

The robust and efficient detection of discontinuities in piecewise continuous functions plays a crucial role in a wide range of computational applications, such as computer-aided design (CAD), computer graphics, and computational fluid dynamics (CFD) [1, 2, 3]. If these discontinuities are not accurately identified and resolved, they can lead to non-physical oscillations, a phenomenon known as the *Gibbs phenomenon* [4].

Several high-order numerical methods, such as the Discontinuous Galerkin (DG) methods [1] and Weighted Essentially Non-Oscillatory (WENO) schemes [5], have been developed to tackle these challenges. These methods excel at handling sharp transitions and maintaining high-order accuracy when solving hyperbolic partial differential equations (PDEs). However, they often encounter difficulties in robustly detecting discontinuities.

In this paper, we present a novel method named *Robust Discontinuity Indicators* (RDI), designed specifically to overcome the limitations of existing methods by providing robust and efficient detection of discontinuities in function values or derivatives, commonly referred to as C^0 and C^1 discontinuities, respectively. RDI is applicable for both node-based and cell-averaged values. We developed RDI by extending the discontinuity indicators in our previous work [6], where the analysis was more heuristic and high-level. We present a more rigorous analysis, including the derivation of the thresholds, and enhance the robustness of the indicators for detecting discontinuities on non-uniform meshes.

RDI is particularly notable for its ability to support general surfaces with complex features, such as boundaries, sharp ridges, and corners, which are common in practical applications [2]. This versatility of RDI opens up new possibilities for its application in computational physics and beyond. By accurately detecting and characterizing discontinuities, RDI offers improved approximation and analysis of piecewise continuous functions, enabling more reliable simula-

tions, data remapping, and other computational tasks. The development of RDI fills a critical gap in the field, providing a powerful tool for handling discontinuities and mitigating the adverse effects of the Gibbs phenomena.

The remainder of the paper is organized as follows: Section 2 provides a brief review of weighted least squares approximations and the Gibbs phenomena. Section 3 analyzes overshoots and undershoots near discontinuities, leading to the derivation of element-based indicators. Section 4 introduces node-based markers using a dual-thresholding strategy and discusses their applicability to non-uniform meshes and surfaces with boundaries and sharp features. Section 5 presents several numerical experiments to demonstrate the robustness of RDI and compares it with alternative approaches. Finally, Section 6 concludes the paper with a summary of the findings and possible future research directions.

2. Background and Preliminaries

Weighted least square (WLS) is a powerful method used in data fitting, remapping, reconstruction, etc. However, degree- p WLS with $p \geq 2$, can introduce oscillations near discontinuities [6]. Interestingly, these oscillations can also be useful in detecting discontinuities. In this section, we provide an overview of WLS and discuss the phenomenon of oscillations, commonly referred to as the Gibbs phenomenon.

2.1. Related work

Discontinuities often lead to undesired overshoots or undershoots in numerical methods. Specifically, C^0 discontinuities, also known as edges [7], jump discontinuities [8, 9] or faults [10, 11], tend to cause $O(1)$ oscillations that persist with mesh refinement [6]. This phenomenon is referred to the Gibbs or Gibbs-Wilbraham phenomenon in the context of the Fourier transform [9]. While C^0 discontinuities have been extensively studied, less attention has been given to C^1 discontinuities, which are discontinuities in the gradients of functions. Nonetheless, C^1 discontinuities are still crucial in various applications. For instance,

they often represent junctions or intersections of components, such as features or ridge points. The C^1 discontinuities may cause mild oscillations in numerical methods [12].

Detecting these discontinuities is essential for the effective resolution of the Gibbs phenomenon in numerical methods. It also has significant implications for various other applications, such as mesh reconstruction [13] and image processing [14]. Several methods have been developed for edge detection, such as the minmod edge detection (MED) [15, 16] based on the polynomial annihilation technique [17], zero-crossing in the second derivatives [18, 19, 20] and the singularity detection and processing with wavelets (SDPW) [21] based on wavelet transform. Among these methods, MED focuses on a 2D unstructured mesh rather than pure image processing. It approximates the jump function to detect the C^0 discontinuities and utilizes MED on an approximation of the gradient to detect the C^1 discontinuities. However, the approximation of gradient near the C^1 discontinuities may diffuse and result in an oscillated smooth function, leading to some false negatives in the detection. In Section 5.2, we will compare our method with MED.

2.2. Weighted-least-squares approximations

In numerical analysis, *approximation* refers to using a simple function to simulate a more complex function or a function without an analytic formula. In practice, these functions might only have values at a discrete set of points, which necessitates the use of *interpolation* to obtain an approximation from these sample points. Degree- p weighted least square is a powerful method that employs polynomials of degree up to p to approximate a function sampled at discrete points. Taking degree-2 WLS as an example, we can expand the n -dimensional Taylor series of a function f at a point $\mathbf{x} = \mathbf{x}_0 + \mathbf{h}$ using the first three terms,

$$f(\mathbf{x}_0 + \mathbf{h}) = f(\mathbf{x}_0) + \mathbf{h}^T \nabla f(\mathbf{x}_0) + \frac{1}{2} \mathbf{h}^T \mathbf{H} f(\mathbf{x}_0) \mathbf{h} + \mathcal{O}(\|\mathbf{h}\|^3), \quad (1)$$

where ∇ and \mathbf{H} denote the gradient and Hessian operators, respectively.

By considering the approximation $f_Q(\mathbf{x}) = f(\mathbf{x}_0) + \mathbf{h}^T \tilde{\mathbf{g}} + \frac{1}{2} \mathbf{h}^T \tilde{\mathbf{H}} \mathbf{h}$, where $\tilde{\mathbf{g}}$ and $\tilde{\mathbf{H}}$ denote the approximations to $\nabla f(\mathbf{x}_0)$ and $\mathbf{H}f(\mathbf{x}_0)$, respectively, we can express each component of $\tilde{\mathbf{g}}$ and $\tilde{\mathbf{H}}$ as a linear combination of $f_i = f(\mathbf{x}_i)$, i.e.,

$$\tilde{g}_j = \sum_k c_{jk} f_k \quad \text{and} \quad \tilde{h}_{ij} = \sum_k d_{ijk} f_k.$$

Here, c_{jk} and d_{ijk} are coefficients that depend on the weights used in the WLS approximation. These coefficients have magnitudes of $\Theta(1/h)$ and $\Theta(1/h^2)$, respectively, and are independent of the function f . When f is at least C^2 continuous, the quadratic WLS approximation $f_Q(\mathbf{x})$ is at least second-order accurate. To determine the coefficients, we construct a linear system

$$\mathbf{A}\mathbf{c} = \mathbf{f},$$

where \mathbf{A} is the generalized Vandermonde matrix and \mathbf{c} contains the coefficients to be determined. By including an adequate number of sampling points in the stencil, we ensure the well conditioning of the generalized Vandermonde matrix after scaling. We assign weights to each equation to emphasize the importance of the corresponding sample point while minimizing the least square of the residual $\|\mathbf{W}(\mathbf{A}\mathbf{c} - \mathbf{f})\|_2$. Different weight choices, such as distance-inverse weights [22] or radial basis function (RBF) weights [23] based on distances, have been used in WLS, each suited for different scenarios. Notably, the WLS-WENO weights [24, 25, 26, 27, 28] are based on function values and aim to resolve discontinuities.

Definition 1. A degree- p WLS is *stable* if the scaled Vandermonde matrix has a bounded condition number independently of h .

Here, h represents the mesh size. Stability is critical in ensuring the accuracy of the approximation under mesh refinement. Note that interpolation is a special case of WLS where the Vandermonde matrix is square.

Lemma 2. Given a C^p function f , of which the $(p+1)$ st derivative is bounded, a stable degree- p WLS f_p is $(p+1)$ st order accurate, i.e.,

$$|f_p - f| = \mathcal{O}(h^{p+1}).$$

We omit the proof since it is similar to the arguments in [22]. Lemma 2 will be used later in Sections 3 and 4 to derive our indicators in RDI.

2.3. Weighted averaging of local fittings

In this subsection, we review the concept of *Weighted Averaging of Local Fittings* (WALF) [29], a technique for reconstructing functions on discrete surfaces $\Omega \subset \mathbb{R}^3$. Given a point \mathbf{p} located within an element with vertices $\{\mathbf{x}_i\}_{i=1}^m$, let $\boldsymbol{\xi}$ denote the natural coordinates of \mathbf{p} such that $\mathbf{p} = \sum_{i=1}^m \xi_i \mathbf{x}_i$. For each vertices \mathbf{x}_i , we obtain an approximation $g_i(\mathbf{p})$ by employing WLS fitting on the projected function $f_i(\mathbf{u}) := f(\mathbf{x})$ defined on Ω , where $\mathbf{u} = \phi_i(\mathbf{x}) \in \mathbb{R}^2$ represents the projection of \mathbf{x} onto the normal plane at \mathbf{x}_i , with \mathbf{x}_i serving as the origin of the local coordinate system. The WALF reconstruction for \mathbf{p} is then given by

$$g_{\text{WALF}}(\mathbf{p}) = \sum_{i=1}^m \xi_i g_i(\mathbf{p}). \quad (2)$$

For further details on WALF, we refer readers to [29].

To construct the WLS approximation g_i for each sampled point \mathbf{x}_i , we use the Buhmann weights in [6, 30]. These weights are solely determined by the distance and are independent of the function values. By precomputing g_i using this approach, we can reuse g_i for all the points in the proximity of \mathbf{x}_i . Compared to pure WLS and the *Continuous Moving Frames* (CMF) method [29, 31], where a separate WLS approximation is constructed for each target point, WALF offers computational advantages when the number of sampled points is smaller than the number of target points. However, it is important to note that WALF is more susceptible to oscillations near discontinuities than CMF, as demonstrated in [29]. This oscillatory property of WALF turns out to be useful in detecting discontinuities, as we will discuss in Section 3.3.

3. Element-Based Indicators

Our technique shares similarities with that of Li et al. [6]. However, the discussions in [6] were relatively high level. We present a more rigorous analysis,

including the derivation of the thresholds.

3.1. Asymptotic bounds in smooth regions

Consider a function f defined over a surface mesh Ω embedded in \mathbb{R}^3 . To derive discontinuity indicators, we start with establishing asymptotic bounds that quantify the difference between stable quadratic polynomial fitting and stable linear interpolation. These bounds provide insights into the accuracy of our approach and its ability to capture smooth variations in the underlying function.

Proposition 3. *In C^2 regions of a piecewise smooth function over a surface mesh Ω , the difference between stable quadratic WLS and stable linear interpolation is $\mathcal{O}(h^2)$.*

Proof. Without loss of generality, let us first assume Ω is composed of triangles. Let $f_L(\mathbf{x}) : \Omega \rightarrow \mathbb{R}$ and $f_Q(\mathbf{x}) : \Omega \rightarrow \mathbb{R}$ denote the linear interpolation and quadratic WLS of a C^2 function f , respectively.

$$|f_L - f_Q| = |(f_L - f) - (f_Q - f)| \leq |f_L - f| + |f_Q - f|, \quad (3)$$

where $|f_L - f| = \mathcal{O}(h^2)$ and $|f_Q - f| = \mathcal{O}(h^3)$ if f is C^2 , as per Lemma 2. Therefore, $|f_L - f_Q| = \mathcal{O}(h^2)$. If the mesh is composed of quadrilaterals, we can replace linear interpolation with bilinear interpolation, and the error bounds still hold. \square

Remark 4. Even if we replace quadratic WLS with a different degree polynomial—be it linear, cubic, or of a higher degree—Proposition 3 still holds true. This is because the error term in the proposition is primarily dictated by the linear interpolation. However, we specifically choose quadratic WLS for its balance of effectiveness and efficiency. While linear WLS does not introduce oscillations, which are necessary for identifying discontinuities, higher-degree WLS methods can increase computational costs. As such, quadratic WLS presents the optimal degree choice; it is the lowest-degree WLS method capable of introducing oscillations, and yet it does so without significantly escalating computational burden. This balance enables us to detect discontinuities more efficiently.

3.2. Asymptotic bounds near discontinuities

The analysis becomes more complex when a function has discontinuities. The derivative of a C^0 function is a Heaviside function, and the derivative of a Heaviside function at the discontinuity equates to a Dirac delta function in a distribution sense. Although such a generalized notion could be used within the context of Taylor series, it is insufficient to employ the Taylor series alone to derive the error bounds. Generalizing the analysis in Section 2.2, we derive the error bounds as follows.

Proposition 5. *In a neighborhood of C^0 and C^1 discontinuities of a piecewise-smooth function, the difference between quadratic WLS and linear interpolation is $\mathcal{O}(1)$ and $\mathcal{O}(h)$, respectively, where h denotes an edge-length measure.*

Proof. First, we consider C^0 discontinuities, i.e., discontinuities in function values. If \mathbf{x}_0 is close to a C^0 discontinuity, we can find a point \mathbf{x}_* on the discontinuity such that $|f(\mathbf{x}_0) - f(\mathbf{x}_*)| = \mathcal{O}(h)$. For any point \mathbf{x} in the vicinity of \mathbf{x}_0 , depending on whether \mathbf{x}_* is on the same side of the discontinuity as \mathbf{x}_0 , we have $|f(\mathbf{x}) - f(\mathbf{x}_*)| = \mathcal{O}(h)$ or $\mathcal{O}(1)$. Hence,

$$\begin{aligned} |f_Q(\mathbf{x}) - f(\mathbf{x})| &= |(f_Q(\mathbf{x}) - f(\mathbf{x}_0)) - (f(\mathbf{x}) - f(\mathbf{x}_*)) + (f(\mathbf{x}_0) - f(\mathbf{x}_*))| \\ &\leq |f_Q(\mathbf{x}) - f(\mathbf{x}_0)| + |f(\mathbf{x}) - f(\mathbf{x}_*)| + |f(\mathbf{x}_0) - f(\mathbf{x}_*)|. \end{aligned}$$

Owing to the $\mathcal{O}(1)$ jump, $\max_{i,j} \{|f_i - f_j|\} = \mathcal{O}(1)$. The gradient and Hessian of the WLS fitting are bounded by $\tilde{\mathbf{g}} = \mathcal{O}(h^{-1})$ and $\tilde{\mathbf{H}} = \mathcal{O}(h^{-2})$, respectively. Therefore,

$$|f_Q(\mathbf{x}) - f(\mathbf{x}_0)| = \left| \mathbf{h}^T \tilde{\mathbf{g}} + \frac{1}{2} \mathbf{h}^T \tilde{\mathbf{H}} \mathbf{h} \right| = \mathcal{O}(1),$$

and in turn

$$|f_Q(\mathbf{x}) - f(\mathbf{x})| \leq |f_Q(\mathbf{x}) - f(\mathbf{x}_0)| + \mathcal{O}(1) = \mathcal{O}(1).$$

Second, if \mathbf{x}_0 is close to a C^1 discontinuity, i.e., discontinuities in derivatives, for any point \mathbf{x} in the vicinity of \mathbf{x}_0 , we can find a point \mathbf{x}_* on the discontinuity such that $|f(\mathbf{x}_0) - f(\mathbf{x}_*)| = \mathcal{O}(h)$ and $|f(\mathbf{x}) - f(\mathbf{x}_*)| = \mathcal{O}(h)$. Due to the

discontinuities, $\max_{i,j} \{|f_i - f_j|\} = \mathcal{O}(h)$. Hence, the gradient and Hessian of the WLS fitting are $\tilde{\mathbf{g}} = \mathcal{O}(1)$ and $\tilde{\mathbf{H}} = \mathcal{O}(h^{-1})$, respectively, and

$$|f_Q(\mathbf{x}) - f(\mathbf{x}_0)| = \left| \mathbf{h}^T \tilde{\mathbf{g}} + \frac{1}{2} \mathbf{h}^T \tilde{\mathbf{H}} \mathbf{h} \right| = \mathcal{O}(h),$$

Therefore,

$$|f_Q(\mathbf{x}) - f(\mathbf{x})| \leq |f_Q(\mathbf{x}) - f(\mathbf{x}_0)| + |f(\mathbf{x}) - f(\mathbf{x}_*)| + |f(\mathbf{x}_0) - f(\mathbf{x}_*)| = \mathcal{O}(h).$$

□

Proposition 6. *The difference between quadratic polynomial fitting and linear interpolation reaches $\Theta(1)$ and $\Theta(h)$ at some points near C^0 and C^1 discontinuities, respectively.*

Proof. The full proof follows a similar logic to Proposition 5 but requires decomposing the function f in terms of discontinuity behavior and careful selection of suitable points \mathbf{x}_0 for the analysis.

Let us first consider a function f with C^0 discontinuities. For convenience, we can decompose it into two components: one with and one without discontinuities, respectively. Specifically, we express f as $f = f^0 + f^1$, where f^0 contains C^0 discontinuities and f^1 is C^0 continuous. We represent the quadratic polynomial fitting and linear interpolation of f at a point \mathbf{x} as $q(\mathbf{x} : f)$ and $l(\mathbf{x} : f)$, respectively. Hence, we have

$$q(\mathbf{x} : f) = q(\mathbf{x} : f^0) + q(\mathbf{x} : f^1)$$

and

$$l(\mathbf{x} : f) = l(\mathbf{x} : f^0) + l(\mathbf{x} : f^1).$$

Let us consider $\mathbf{x}_0 \in e_0$, a point near C^0 discontinuities, such that the element e_0 does not cover any C^0 discontinuities region, but the stencil of \mathbf{x}_0 does. The quadratic polynomial fitting at \mathbf{x}_0 can be expressed as

$$q(\mathbf{x}_0 : f) = \sum_{i=1}^n c_i f_i,$$

where $f_i = f(\mathbf{x}_i)$ denotes the function value at the stencil $\{\mathbf{x}_i\}_{i=1}^n$ of \mathbf{x}_0 and c_i is related only to the position of \mathbf{x}_0 and its stencil $\{\mathbf{x}_i\}_{i=1}^n$.

Assuming that the mesh is fine enough to contain only one C^0 discontinuity in the stencil, i.e., we can decompose f in a small neighborhood Λ of \mathbf{x}_0 such that

$$f^0(\mathbf{x}) = \begin{cases} \lambda, & \text{if } \mathbf{x} \in \Gamma, \\ 0, & \text{if } \mathbf{x} \in \Lambda \setminus \Gamma, \end{cases}$$

where $\lambda \neq 0$ is a constant approximating the jump of the C^0 discontinuity. Either $e_0 \subset \Gamma$ or $e_0 \subset \Lambda \setminus \Gamma$. For the former case, we choose a new $\tilde{f}^0 = \lambda - f^0$. It is sufficient to set the non-zero region Γ of f^0 to satisfy that $e_0 \cap \Gamma = \emptyset$. Consequently,

$$l(\mathbf{x}_0 : f^0) = 0.$$

Because a C^0 discontinuity exists, $\{\mathbf{x}_i\}_{i=1}^n \cap \Gamma \neq \emptyset$. Denoting $K = \{i | \mathbf{x}_i \in \Gamma, 1 \leq i \leq n\}$, we get

$$q(\mathbf{x}_0 : f^0) = \sum_{i \in K} c_i f_i^0 = \lambda \sum_{i \in K} c_i.$$

In a local neighborhood, Γ is fixed. By moving \mathbf{x}_0 such that the cardinality of K is one, $\#K = 1$, we have $\sum_{i \in K} c_i \neq 0$. Consequently,

$$q(\mathbf{x}_0 : f^0) = \lambda \sum_{i \in K} c_i = \Theta(1).$$

According to Proposition 5,

$$q(\mathbf{x} : f^1) - l(\mathbf{x} : f^1) = O(h),$$

and therefore

$$q(\mathbf{x} : f) - l(\mathbf{x} : f) = \Theta(1) + O(h) = \Theta(1).$$

Secondly, if \mathbf{x} is near a C^1 discontinuity, we decompose f in a local neighborhood of \mathbf{x} as $f = f^2 + f^3$, where f^2 is C^0 continuous but contains C^1 discontinuities, and f^3 is C^2 continuous. Assuming the mesh is fine enough to

have only one C^1 discontinuity in the stencil, we can find a decomposition of f so that

$$f^2(x) = \begin{cases} \Theta(h), & \mathbf{x} \in \Gamma \\ 0, & \text{otherwise} \end{cases},$$

where Γ is fixed in a local region and $e_0 \cap \Gamma = \emptyset$. Consequently, we have $l(\mathbf{x}_0 : f^2) = 0$. In a similar manner, by finding an \mathbf{x}_0 such that the cardinality of $K = \{i | \mathbf{x}_i \in \Gamma, 1 \leq i \leq n\}$ is one, we have

$$q(\mathbf{x}_0 : f^2) = \sum_{i \in K} c_i f_i^2 = \Theta(h).$$

According to Proposition 3, $q(\mathbf{x} : f^3) - l(\mathbf{x} : f^3) = O(h^2)$, and thus,

$$q(\mathbf{x} : f) - l(\mathbf{x} : f) = \Theta(h) + O(h^2) = \Theta(h).$$

This completes the proof of the proposition. \square

It is important to note that the bounds in Proposition 5 represent upper limits. In practice, the differences may be significantly smaller at certain points, so discontinuity indicators may yield false negatives near such points, which we will address in Section 4.

3.3. Precomputing operator for cell-based overshoot-undershoot indicators

Overshoot-undershoot indicator

We first build an operator to compute cell-based indicators for local overshoots and undershoots, which are inspired by Proposition 5. For a cell σ , let $g_{\sigma,1}$ and $g_{\sigma,2}$ denote the approximate values at the “cell center” of σ from linear interpolation and quadratic WALF, respectively. We compute a value α_σ as the difference between $g_{\sigma,2}$ and $g_{\sigma,1}$, that is,

$$\alpha_\sigma = g_{\sigma,2} - g_{\sigma,1}. \quad (4)$$

We refer to α_σ as the *overshoot-undershoot (OSUS) indicator* at σ , since its positive and negative sign respectively indicates local overshoot and undershoot of $g_{\sigma,2}$ at σ , and its magnitude indicates the level of overshoot or undershoot.

We compute the cell center by simply averaging the nodes of σ . Note that this point is not necessarily the centroid in general. We choose this point to compute $g_{\sigma,\cdot}$ because $g_{\sigma,1}$ is essentially the average of corresponding nodal values, and more importantly, $g_{\sigma,2}$ is prone to overshoot and undershoot more significantly at this point than at points closer to nodes.

Both $g_{\sigma,2}$ and $g_{\sigma,1}$ are weighted sums of nodal values, and so is α_σ . Consequently, the computation of the α values for all the cells can be expressed as a sparse matrix-vector multiplication. We refer to this sparse matrix as the *OSUS operator*. Each row of the operator corresponds to a cell center, each column corresponds to a node in the mesh, and each nonzero entry stores a nonzero weight. Specifically, we compute the quadratic WALF using the 1.5-ring stencil at each node of the cell [29], and hence the nonzeros in each row for a cell σ would correspond to the union of the 1.5-rings of the nodes of σ . This RDI operator only depends on the mesh and is independent of the function values, so it can be pre-computed for a given mesh.

Its computation requires a data structure that supports computing the k -ring neighborhood of nodes, and we implement it using an array-based half-facet data structure [32]. Occasionally, for some poorly shaped meshes, the Vandermonde matrix from WALF may be ill-conditioned. When this happens, we monitor the condition number of the Vandermonde matrix and enlarge the stencils for ill-conditioned systems.

Element-based threshold

In accordance with Propositions 3, 5, and 6, most of the smooth regions can be filtered out by an element-wise threshold

$$\tau_\sigma = \max \left\{ \underbrace{C_\ell \delta f_\ell h_\ell^{0.5}}_{\tau_\ell}, \underbrace{C_g \delta f_g h_g^{1.5}}_{\tau_g} \right\}, \quad (5)$$

where δf_ℓ represents the local range of f within the k -ring neighborhood for WALF reconstruction, h_ℓ is the local average edge length in the local uv coordinate system, and δf_g denotes the global range of function over the mesh,

and h_g denotes a global measure of average edge length in the xyz coordinate system. C_ℓ and C_g are two parameters, which we determine empirically. All the elements with $|\alpha_\sigma| > \tau_\sigma$ would be marked. However, some elements at the peak might also be marked, leading to false positives. We will further filter out these false positives using the node-based indicator in Section 4.

4. Node-based Markers via Dual Thresholding

In Section 3.3, we defined an element-based indicator to exclude most of the smooth region. However, using solely the element-based indicator may lead to false positives, particularly in the vicinity of local extremes on coarse meshes. To mitigate this issue, we propose a *dual-thresholding* approach using node-based markers.

4.1. Properties of α_σ near local extremes

To derive more accurate indicators, we need a more precise estimation of α_σ . In the following, we derive the theory first in \mathbb{R}^2 and then generalize it to surfaces.

Proposition 7. *In the C^2 regions of a piecewise smooth function, α_σ is negative near a local minimum and positive near a local maximum on a sufficiently fine mesh of a plane.*

Proof. Without loss of generality, we assume the mesh is composed of triangles. Consider a function $f : \mathbb{R}^2 \rightarrow \mathbb{R}$ defined on a plane. For a triangular element $\sigma = \mathbf{x}_1\mathbf{x}_2\mathbf{x}_3$ within the C^2 region of f , we obtain the linear interpolation $g_{\sigma,1}$ and the WALF reconstructed value $g_{\sigma,2}$ from (2) as follows:

$$g_{\sigma,1} = \frac{1}{3} \sum_{i=1}^3 f(\mathbf{x}_i) \quad \text{and} \quad g_{\sigma,2} = \frac{1}{3} \sum_{i=1}^3 f_i(\mathbf{x}_0),$$

where $\mathbf{x}_0 = \frac{1}{3}(\mathbf{x}_1 + \mathbf{x}_2 + \mathbf{x}_3)$ is the cell center of σ and f_i is the degree-2 WLS

centered at \mathbf{x}_i . Hence, we obtain

$$\begin{aligned}
\alpha_\sigma &= g_{\sigma,2} - g_{\sigma,1} \\
&= \frac{1}{3} \sum_{i=1}^3 f_i(\mathbf{x}_0) - \frac{1}{3} \sum_{i=1}^3 f(\mathbf{x}_i) \\
&= \frac{1}{3} \sum_{i=1}^3 (f_i(\mathbf{x}_0) - f(\mathbf{x}_0)) + f(\mathbf{x}_0) - \frac{1}{3} \sum_{i=1}^3 f(\mathbf{x}_i) \\
&= f(\mathbf{x}_0) - \frac{1}{3} \sum_{i=1}^3 f(\mathbf{x}_i) + O(h^3).
\end{aligned} \tag{6}$$

The last equality above holds because of Lemma 2. Let (ξ, η) denote the natural coordinates of σ . Then,

$$\mathbf{x}(\xi, \eta) = \mathbf{x}_1 + \xi \boldsymbol{\mu}_1 + \eta \boldsymbol{\mu}_2,$$

where $\boldsymbol{\mu}_1 = \mathbf{x}_2 - \mathbf{x}_1$, $\boldsymbol{\mu}_2 = \mathbf{x}_3 - \mathbf{x}_1$ are the two edges of e . The Taylor series expansion [33] of f on \mathbf{x}_1 is

$$f(\mathbf{x}(\xi, \eta)) = f(\mathbf{x}_1) + (\xi \boldsymbol{\mu}_1 + \eta \boldsymbol{\mu}_2)^T \nabla f + \frac{1}{2} (\xi \boldsymbol{\mu}_1 + \eta \boldsymbol{\mu}_2)^T \tilde{\mathbf{H}} (\xi \boldsymbol{\mu}_1 + \eta \boldsymbol{\mu}_2) + O(h^3), \tag{7}$$

where $\tilde{\mathbf{H}}$ is the Hessian matrix of f at \mathbf{x}_1 . Substituting the terms in (6) with (7), we obtain

$$\begin{aligned}
\alpha_\sigma &= \frac{1}{2} \left[\left(\frac{1}{3} \boldsymbol{\mu}_1 + \frac{1}{3} \boldsymbol{\mu}_2 \right)^T \tilde{\mathbf{H}} \left(\frac{1}{3} \boldsymbol{\mu}_1 + \frac{1}{3} \boldsymbol{\mu}_2 \right) - \frac{1}{3} \boldsymbol{\mu}_1^T \tilde{\mathbf{H}} \boldsymbol{\mu}_1 - \frac{1}{3} \boldsymbol{\mu}_2^T \tilde{\mathbf{H}} \boldsymbol{\mu}_2 \right] + O(h^3) \\
&= -\frac{1}{18} (\boldsymbol{\mu}_1^T \tilde{\mathbf{H}} \boldsymbol{\mu}_1 + \boldsymbol{\mu}_2^T \tilde{\mathbf{H}} \boldsymbol{\mu}_2 + \boldsymbol{\mu}_3^T \tilde{\mathbf{H}} \boldsymbol{\mu}_3) + O(h^3),
\end{aligned} \tag{8}$$

where $\boldsymbol{\mu}_3 := \boldsymbol{\mu}_2 - \boldsymbol{\mu}_1 = \mathbf{x}_3 - \mathbf{x}_2$ is the third edge of e . Note that $\boldsymbol{\mu}_i = O(h)$, so the first term in (8) is the dominant term. The Hessian matrix is positive definite near a local minimum and negative-definite near a local maximum, so α_σ will be negative and positive, respectively, when h is sufficiently small. \square

In Section 4.2, we will utilize the property above to differentiate the smooth region near extremes from discontinuities with alternating signs of α_σ . To apply it to surface meshes, however, we need to generalize the result to surfaces. We assume the vertices interpolate the piecewise smooth surface.

Proposition 8. *Within the intersection of C^2 regions of a piecewise smooth function and G^2 regions of the surface, the α_σ are negative near a local minimum and positive near a local maximum, provided that the mesh of the surface is sufficiently fine.*

Proof. Let us consider a function $f : \Omega \rightarrow \mathbb{R}$ defined on a general surface Ω . Within a G^2 region of Ω , suppose there is a triangular element $\sigma = v_1 v_2 v_3$. We construct three smooth projections, $p_k : \mathbb{R}^3 \rightarrow \Omega$, from the normal plane of v_k to a small neighborhood Φ_k of v_k for $k = 1, 2, 3$. We assume the mesh is fine enough so that $\sigma \subset \Phi_k, k = 1, 2, 3$. Additionally, we construct another projection $q_k : \mathbb{R}^2 \rightarrow \mathbb{R}^3$ from \mathbb{R}^2 to the normal plane, keeping the distance preserved. That is,

$$\|\mathbf{x}_1 - \mathbf{x}_2\|_2 = \|q_k(\mathbf{x}_1) - q_k(\mathbf{x}_2)\|_2, \forall \mathbf{x}_1, \mathbf{x}_2 \in \mathbb{R}^2, 1 \leq k \leq 3.$$

Let \mathbf{x}_i^k be the corresponding vertex of v_i for p_k and q_k on \mathbb{R}^2 . It then follows that $p_k(q_k(\mathbf{x}_i^k)) = v_i$ for $i = 1, 2, 3$. The WALF reconstructed value is then given by

$$g_{\sigma,2} = \frac{1}{3} \sum_{i=1}^3 f_i(v_0),$$

where v_0 is the cell center of σ , and f_i is the degree-2 WLS centered at v_i . Let $\tilde{f}_k(\mathbf{x}) := f_k(p_k(q_k(\mathbf{x})))$, and α_σ is then given by

$$\begin{aligned} \alpha_\sigma &= g_{\sigma,2} - g_{\sigma,1} \\ &= \frac{1}{3} \sum_{k=1}^3 f_k(v_0) - \frac{1}{3} \sum_{i=1}^3 f(v_i) \\ &= \frac{1}{3} \sum_{k=1}^3 (\tilde{f}_k(\mathbf{x}_0^k) - \frac{1}{3} \sum_{i=1}^3 \tilde{f}_k(\mathbf{x}_i^k)) - \frac{1}{3} \sum_{i=1}^3 (f(v_i) - \frac{1}{3} \sum_{k=1}^3 \tilde{f}_k(\mathbf{x}_i^k)), \end{aligned} \quad (9)$$

where $\mathbf{x}_0^k = \frac{1}{3}(\mathbf{x}_1^k + \mathbf{x}_2^k + \mathbf{x}_3^k), \forall 1 \leq k \leq 3$. Since the vertices are on the piecewise smooth surface, we can apply Lemma 2 and conclude that the second term in (9) is $O(h^3)$.

Following the argument as in Proposition (7), we then get:

$$\tilde{f}_k(\mathbf{x}_0^k) - \frac{1}{3} \sum_{i=1}^3 \tilde{f}_k(\mathbf{x}_i^k) = -\frac{1}{18} \sum_{i=1}^3 (\boldsymbol{\mu}_i^k)^T \tilde{\mathbf{H}}_k \boldsymbol{\mu}_i^k + O(h^3), \quad (10)$$

where $\tilde{\mathbf{H}}_k$ is the Hessian matrix for \tilde{f}_k at \mathbf{x}_k^k and $\boldsymbol{\mu}_i^k$ are the edges for the triangle in the domain of \tilde{f}_k . The local extremes of f in Ω correspond to local extremes of \tilde{f}_k in \mathbb{R}^2 . Hence, the $\tilde{\mathbf{H}}_k$ are either all positive definite or all negative definite, at the same time. Therefore, the proposition has been proved. \square

4.2. Computing node-based oscillation indicators

Definition of oscillation indicator

Given the nodal values of a function f , we first calculate of the cell-based α values by multiplying the OSUS operator with a vector composed of nodal function values. However, since the $\mathcal{O}(1)$ and $\mathcal{O}(h)$ estimates in Proposition 5 merely provide the upper bounds of α_σ , these values may be arbitrarily small at some isolated cells near discontinuities. As a result, the OSUS indicators alone are insufficiently reliable for detecting discontinuities. To enhance robustness, we further process the OSUS indicators to generate node-based *oscillation indicators*.

Specifically, for a given node v , we compute its oscillation indicator from the adjacent nodes using the formula:

$$\beta_v = \frac{\sum_{\sigma \ni v} w_\sigma |\alpha_\sigma - \bar{\alpha}_v|}{(\sum_{\sigma \ni v} w_\sigma) (|\bar{\alpha}_v| + \epsilon_\beta \max_{\sigma \ni v} |\alpha_\sigma|) + \epsilon_{\min}}. \quad (11)$$

Here, $\bar{\alpha}_v$ denotes a weighted average of the α values for the cells incident on v , i.e.,

$$\bar{\alpha}_v = \sum_{\sigma \ni v} w_\sigma \alpha_\sigma / \sum_{\sigma \ni v} w_\sigma,$$

where the weights may be unit weights as [6] or area-based weights. The denominator in (11) comprises safeguards (namely, the second and third terms) against division by a value that is too small, which may happen if the function is locally linear. ϵ_β is a small number, which can be set to 10^{-3} in practice. The last term ϵ_{\min} in the denominator, which is the smallest positive floating-point number (approximately 2.2×10^{-308} for double-precision floating-point numbers), serves as an additional safeguard against division by zero if the input function is a constant. It should be noted that β_v is non-dimensional and is independent of the function value and the mesh scale.

From both a practical and numerical perspective, the definition of β_v is important. Computationally, given the element-based α values, it is efficient to calculate the node-based β values. Numerically, the definition of β_v warrants justification. Suppose that f is sufficiently nonlinear such that $\beta_v \approx \sum_{\sigma \ni v} w_\sigma |\alpha_\sigma - \bar{\alpha}_v| / |\sum_{\sigma \ni v} w_\sigma \alpha_\sigma|$. Firstly, this quantity no longer depends on h . Secondly, the numerator of β_v captures the variation of α_σ , and the denominator further intensifies this variation when α_σ alternates in sign, particularly near C^0 discontinuities. These insights will be useful in the development of an effective thresholding strategy.

Derivation of node-based markers via dual thresholding

As mentioned in Section 2.1, Gibbs phenomena may occur for degree-2 polynomial fitting near C^0 and C^1 discontinuities, leading to oscillations. Linear interpolation would not introduce any $O(1)$ oscillation. Hence, α_σ would be positive in the overshoot region and negative in the undershoot region. Consequently, $\sum_{\sigma \ni v} w_\sigma \alpha_\sigma$ would largely cancel out and be close to 0 in comparison to $\sum_{\sigma \ni v} w_\sigma |\alpha_\sigma|$. As a result, β_v would be large near the discontinuities. In contrast, Proposition 8 suggests that all the α_σ around v would have the same sign near a local extremum of f in the smooth region, resulting in a small β_v . In terms of implementation, we use the 1-ring neighborhood to evaluate β from α . While using a larger neighborhood may improve the precision of the indicator, it will increase computational cost.

To distinguish between discontinuities, we use threshold κ for β_v and devise a *dual-thresholding* strategy. Specifically, we mark a node v as discontinuity if it has a large β value and at least one of its incident elements has a large α value, i.e.,

$$\eta_v = \begin{cases} 1 & \text{if } \beta_v > \kappa \text{ and } \exists e \ni v \text{ s.t. } \alpha_\sigma > \tau_\sigma, \\ 0 & \text{otherwise} \end{cases},$$

where κ is the threshold for β_v and τ_σ is the threshold in Section 3.3.

The threshold κ is determined empirically, selected from the interval $[0.2, 0.5]$ for C^1 discontinuities and $[1, 2]$ for C^0 discontinuities. A lower κ value will

result in a more sensitive indicator but may introduce a higher number of false positives. On the other hand, a higher κ value will yield a stricter indicator, potentially leading to an increase in false negatives. Users can adjust κ_0 and κ_1 for C^0 and C^1 discontinuities, respectively, according to their specific tolerance of false positives and false negatives.

Area weights for non-uniform meshes

On nonuniform meshes, we observe that utilizing unit weights, as in [6] may result in many false positives. For instance, let us assume we have a coarse element σ_0 and several fine elements $\sigma_k, k = 1, 2, \dots, n$ around v at the intersection of C^2 continuous region of f and G^2 regions of the surface. Assume $\|\mathbf{u}_i^0\| = O(h)$ and $\|\mathbf{u}_i^k\| = o(h)$ for all $1 \leq k \leq n$, where \mathbf{u}_i^k are the edges of element σ_k for all $0 \leq k \leq n, 1 \leq i \leq 3$. Based on (9) and (10), we obtain $\alpha_{\sigma_0} = O(h^2)$ and $\alpha_{\sigma_k} = o(h^2)$ for all $1 \leq k \leq n$. With unit weights, we get $\bar{\alpha}_v \approx \frac{1}{n+1}\alpha_{\sigma_0}$, which leads to

$$\beta_v \approx \frac{\sum_{k=0}^n |\alpha_{\sigma_k} - \bar{\alpha}_v|}{|\sum_{k=0}^n \alpha_{\sigma_k}|} \approx \frac{|\alpha_{\sigma_0} - \bar{\alpha}_v| + \sum_{k=1}^n |\bar{\alpha}_v|}{|\alpha_{\sigma_0}|} \approx \frac{2n}{n+1}.$$

In this case, v could erroneously be identified as a C^1 discontinuity node with such a large β_v .

To mitigate such false positives, we employ area weights. Given $w_{\sigma_0} = O(h^2)$ and $w_{\sigma_k} = o(h^2)$ for all $1 \leq k \leq n$, we have $\bar{\alpha}_v \approx \alpha_{\sigma_0}$, yielding

$$\beta_v \approx \frac{w_{\alpha_0}|\alpha_{\sigma_0} - \bar{\alpha}_v| + \sum_{k=1}^n w_{\alpha_k}|\bar{\alpha}_v|}{|w_{\alpha_0}\alpha_{\sigma_0}|} = o(1).$$

As a result, β_v is close to 0, thereby preventing the false positive.

4.3. Generalization to surfaces with geometric discontinuities

Our preceding analysis assumed G^2 continuity of the surface, and hence is not applicable when dealing with geometric discontinuities in normals and curvatures. To accommodate these geometric discontinuities during the detection of numerical discontinuities, we employ virtual splitting as presented in [13] along the ridge curves. Virtual splitting makes the twin half-edges along ridge curves

appear disconnected in the half-facet data structure and in turn, creates a separate connected component for each smooth region. As a result, the stencils in the WLS computations will not include points from different sides of geometric discontinuities. In this work, we focus on discontinuities in normal directions, such as sharp ridges and corners. For instance, after the virtual splitting of a cylinder, the two bases and the lateral surface become three distinct connected components. We then separately run our RDI on these surface patches with boundaries. Without virtual splitting, using RDI might introduce many false positives and negatives, as we demonstrate in Appendix A.

Close to the geometric boundary, whether originally present or created by virtual splitting, we observed that a 3-ring neighborhood provides adequate rows in the Vandermonde matrix for stability while computing the degree-2 WLS in the OSUS operator. Similarly, we could use a 2-ring neighborhood while computing β_v for a vertex on the boundary. These adjustments aid in providing accurate indicator results, as demonstrated in Section 5.3.

4.4. *Summary of algorithm*

We outline the complete algorithm for RDI. Our approach consists of three stages: (1) computation of element-based discontinuity indicators, denoted as α values; (2) calculation of node-based indicators, referred to as β values; and (3) acquisition of node-based discontinuity markers using a novel dual-thresholding strategy.

Our design principle aims to separate offline preprocessing from online computation, as well as separate the data structures. Given a mesh, the offline segment involves computing the OSUS operator, which is performed only when a new mesh is employed. Once the OSUS operator is generated, we execute the rapid online segment, as outlined in Algorithm 1, to detect discontinuities with varying function values on the mesh.

To analyze the time complexity of the algorithm, let us denote the number of vertices as $N = |V|$ and the number of elements as $M = |E|$ for the complete virtual splitting surface. The offline segment, which generates the sparse OSUS

Algorithm 1 Robust Discontinuities Indicator

Require: A surface mesh $\Gamma = (V, E)$ containing the coordinate of vertices V and connectivity table for elements E , the OSUS operator \mathbf{O} generated from Γ , function values \mathbf{f} on all the nodes, two node-based thresholds κ_0, κ_1 for C^0 and C^1 discontinuities, $\kappa_0 > \kappa_1$

Ensure: A vector of integer \mathbf{I} indicating discontinuities on all the nodes

```
1:  $\alpha \leftarrow \mathbf{O}\mathbf{f}$ 
2:  $I_v \leftarrow 0, \forall v \in V$ 
3: for all element  $\sigma \in E$  do ▷ Pre-filtering using  $\alpha$ 
4:   Compute the weight  $w_\sigma$ 
5:   Compute the threshold  $\tau_\sigma$  in (5)
6:   if  $|\alpha_\sigma| > \tau_\sigma$  then
7:      $I_v \leftarrow 1, \forall v \in \sigma$ 
8:   end if
9: end for
10: for all vertex  $v \in V$  do ▷ Resolve false positives
11:   if  $I_v = 1$  then
12:     Compute  $\beta_v$  in (11)
13:     if  $\beta_v > \kappa_0$  then
14:        $I_v \leftarrow 2$ 
15:     else if  $\beta_v \leq \kappa_1$  then
16:        $I_v \leftarrow 0$ 
17:     end if
18:   end if
19: end for
```

operator, incurs a time complexity of $O(N + M)$, counted only once for each mesh.

As for the online part, the complexity of sparse matrix-vector multiplication to compute α is $O(M)$. The pre-filtering using α also has a time complexity of $O(M)$. The process of resolving false positives possesses a time complexity of $O(K)$, where K is the count of elements that pass pre-filtering. When applying a new function on the same mesh, another online part with complexity $O(M)$ is required. For detecting discontinuities of l functions on the same mesh, the overall time complexity is $O(N + (l + 1)M)$.

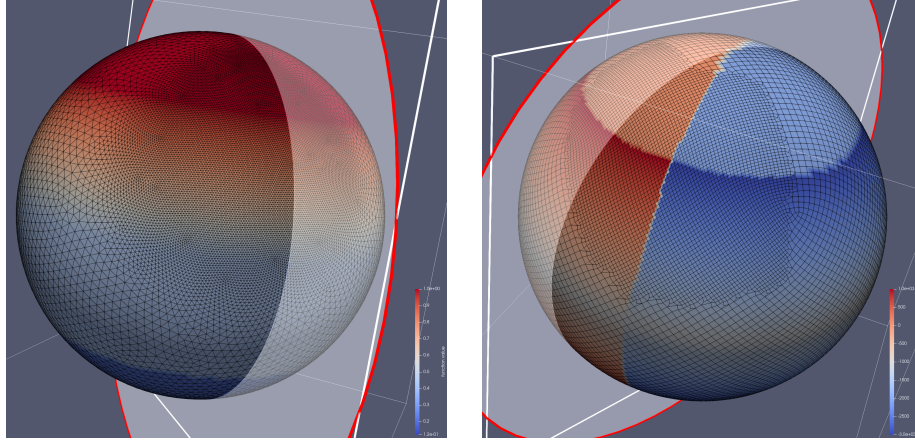
5. Numerical Results

In this section, we report several numerical experiments conducted with RDI, including comparisons on planes, evaluations on general surfaces with sharp features, and the use case of remapping nodal values between meshes for discontinuous functions. We have implemented our algorithms in MATLAB and converted the code into C++ using MATLAB Coder. The numerical experiments were conducted using MATLAB R2022b on Linux. Since one of the key applications of RDI is remapping in climate modeling, which tends to employ various representations of the sphere, some of our experiments use spherical meshes.

5.1. Experimentation on unit spheres with nonuniform meshes

To evaluate our discontinuity indicators, we employ two piecewise smooth functions, “interacting waves” and “crossing waves,” which were previously used in [6]. The definitions of these functions are as follows:

$$f_1(\theta, \varphi) = \begin{cases} 1 & 0 \leq \theta < 5\pi/18 \\ 1.7 - 2.52\theta/\pi & 5\pi/18 \leq \theta < \pi. \\ 0.44 & \pi/2 \leq \theta < 13\pi/18 \\ 0.24 & 13\pi/18 \leq \theta < 9\pi/10 \\ 0.12 & 9\pi/10 \leq \theta \leq \pi \end{cases}, \quad (12)$$



(a) f_1 on the dual of a coarse regionally refined SCVT with the intersection plane $x + y = 0$. (b) f_2 on a coarse regionally refined cubed-sphere with the intersection plane $y - 2x = 0$.

Figure 1: Function values on coarse regionally refined meshes and the intersection planes.

and

$$f_2(\theta, \varphi) = -1000 + 2000 \text{sign}(\cos(\varphi)) \begin{cases} 1/2 & 0 \leq \theta < \pi/4 \\ -4(\theta/\pi - 1/2) & \pi/4 \leq \theta < \pi/2 \\ 4(\theta/\pi - 1/2) & \pi/2 \leq \theta < 3\pi/4 \\ 1 & 3\pi/4 \leq \theta < 7\pi/8 \\ -64\theta^2/\pi^2 + 112\theta/\pi - 48 & 7\pi/8 \leq \theta \leq \pi \end{cases} . \quad (13)$$

Note that f_1 has C^0 and C^1 discontinuities, whereas f_2 has C^0 , C^1 , and C^2 discontinuities. Figure 1 displays the color maps of the two functions on two regionally refined meshes. In particular, f_1 is shown on the dual of a spherical centroidal Voronoi tessellations (SCVT) mesh [34], and f_2 is shown on a cubed-sphere mesh. The meshes in Figure 1 are relatively coarse. For ease of visualization, we intersect the sphere with planes and will depict the values on the intersection curves henceforth.

Figure 2 depicts the function values and β values along the intersection curves on the finer meshes, which have edge lengths of approximately one fourth

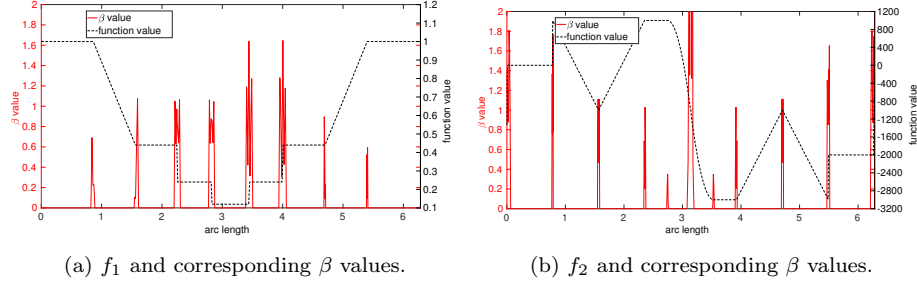


Figure 2: Functions f_1 and f_2 along with their corresponding β values along the cross section of finer regionally refined meshes with intersection planes.

of those seen in Figure 1. It is evident that the β_v values can effectively distinguish the discontinuities from the smooth regions. Figure 3 shows the nodes where $\beta_v \geq 0.5$. These nodes correspond to the regions with C^0 and C^1 discontinuities. Hence, we choose the threshold $\kappa = 0.5$ for detecting discontinuities, as previously mentioned in Section 4.2. Reducing κ to a smaller value may allow for the identification of some C^2 discontinuities on coarse meshes but would also increase the risk of false positiveness.

5.2. Comparison with minmod edge detection

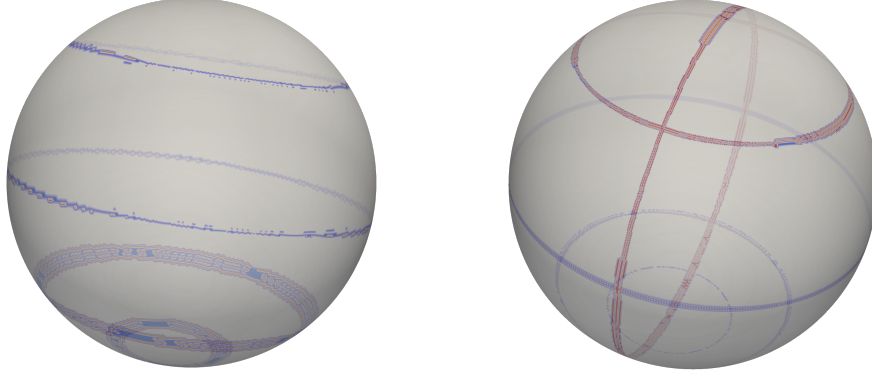
As alluded to in Section 2.2, RDI is closely related to WLS-ENO, which is in turn related to limiters in solving hyperbolic PDEs, such as minmod (see, e.g., [35]). Therefore, we compare RDI with the minmod edge detection (MED) [15, 16]. Since MED is only defined in 2D, we conduct the comparison on planes.

First, we use two test functions, f_3 and f_4 , from [15], both of which contain only C^0 discontinuities. Specifically, function f_3 is given by

$$f_3(x, y) = \begin{cases} xy + \cos(2\pi x^2) - \sin(2\pi x^2), & \text{if } x^2 + y^2 \leq \frac{1}{4}, \\ 10x - 5 + xy + \cos(2\pi x^2) - \sin(2\pi x^2), & \text{if } x^2 + y^2 > \frac{1}{4}, \end{cases}$$

for $-1 \leq x, y \leq 1$, and f_4 is the gray level of the Shepp-Logan phantom [36].

For comparison with [15], we generated 16,384 random points on $[-1, 1] \times [-1, 1]$. As RDI uses a mesh data structure for computing the neighborhood,



(a) Detected discontinuity cells of f_1 on level-3 regionally refined SCVT. (b) Detected discontinuity cells of f_2 on level-3 regionally refined cubed-sphere mesh.

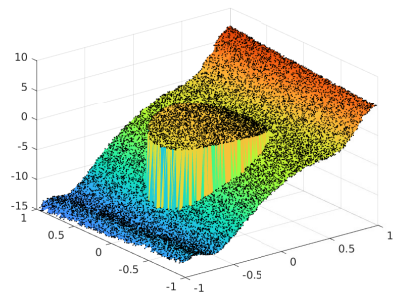
Figure 3: Detected discontinuity cells (the red region) on regionally refined meshes.

we computed the Delaunay triangulation of these points when applying RDI. To visualize the detected discontinuities, we computed an approximation of the local jump function

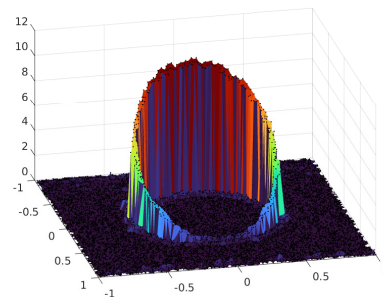
$$\delta f(x) = \begin{cases} \max_{R(x)} f(x) - \min_{R(x)} f(x), & \text{if } x \in D(f), \\ 0, & \text{if } x \notin D(f), \end{cases}$$

where $D(f)$ is the discontinuity region detected by RDI, and $R(x)$ is the 1-ring neighborhood of the point x on the sampled mesh. Figure 4 shows the local jump function, which is similar to Figures 4.2 and 4.3 of MED [15]. However, the detected discontinuities from MED appear to be thinner than those of RDI, since RDI uses larger stencils.

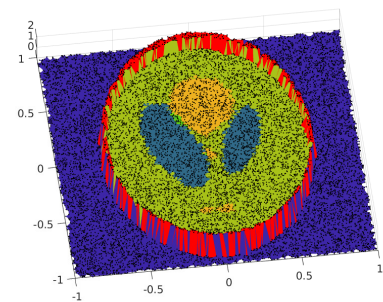
A key feature of RDI, which is also partially the reason for its larger stencils, is that it can detect both C^0 and C^1 discontinuities. In [16], MED was extended to detect C_1 discontinuities by first estimating the derivatives. To compare with



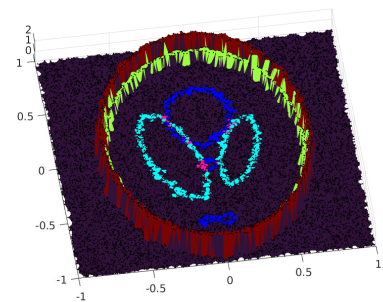
(a) f_3



(b) δf_3



(c) f_4



(d) δf_4

Figure 4: Original functions (a) f_3 and (b) f_4 , and their approximated local jump functions (c) and (d), respectively.

[16], we use the test function f_5 from [16],

$$f_5 = \begin{cases} -(\sqrt{x^2 + y^2} - \frac{1}{2}) + \frac{1}{12} \sin(2\pi\sqrt{x^2 + y^2}), & \text{if } \sqrt{x^2 + y^2} < \frac{1}{2}, \\ (\sqrt{x^2 + y^2} - \frac{1}{2}) + \frac{1}{12} \sin(2\pi\sqrt{x^2 + y^2}), & \text{if } \sqrt{x^2 + y^2} \geq \frac{1}{2}, \end{cases}$$

which has a C_1 discontinuity at the origin and along the unit circle. We generated three different meshes over $[-1, 1] \times [-1, 1]$ of similar sizes as those in [16], including one uniform mesh and two irregular meshes. As shown in Figure 5, RDI detected all the C^1 discontinuities similar to MED, except for the discontinuities at the center over the uniform mesh. It is worth noting that RDI produced fewer false positives than those in [16], probably because the WLS scheme used in RDI is less prone to noise. In addition, RDI is potentially more efficient than MED, since the most expensive part of RDI, namely the OSUS operator, is independent of the function values and hence can be constructed in an offline preprocessing step. In contrast, the operators in MED depend on function values and cannot be evaluated offline.

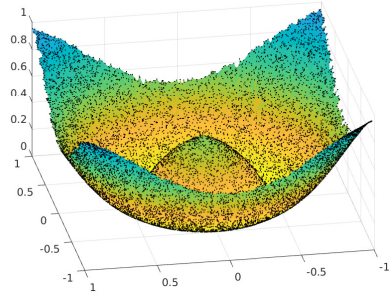
5.3. Generalization to surfaces with sharp features

Our previous examples employed simple smooth geometries, such as spheres and planes. We now consider surfaces with sharp features, which present additional complications. Similar to [13], we virtually split the surface mesh into smooth patches along the feature curves and then employ one-sided stencils along the sharp features. The virtual splitting help prevent many false positives and negatives, as we demonstrate in Appendix A. To maintain stability, we increase the stencil sizes near the patch boundaries when computing the OSUS operator, as discussed in Section 4.3.

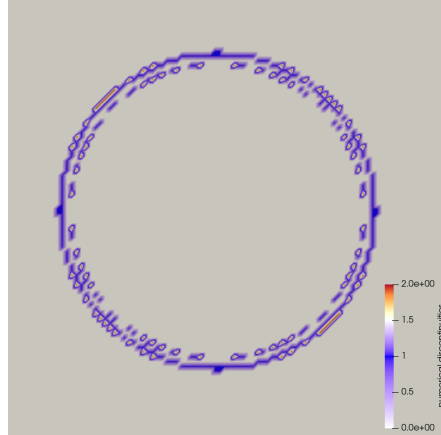
We carried out several experiments and displayed the results of scaled functions f_6 and f_7 , which are defined as

$$f_6(x, y, z) = \tanh(x)\text{sign}(y) + \tanh(y)\text{sign}(z) + \tanh(z)\text{sign}(x),$$

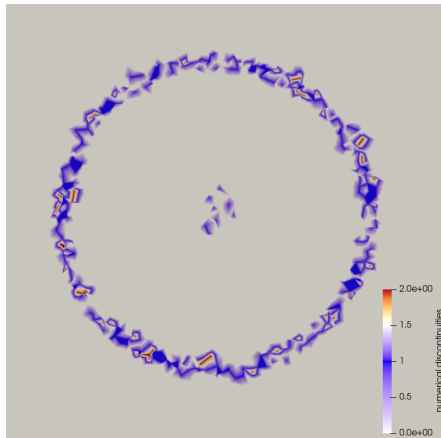
$$f_7(x, y, z) = (\max\{x\} - \min\{x\})g\left(\frac{x - \min\{x\}}{\max\{x\} - \min\{x\}}\right),$$



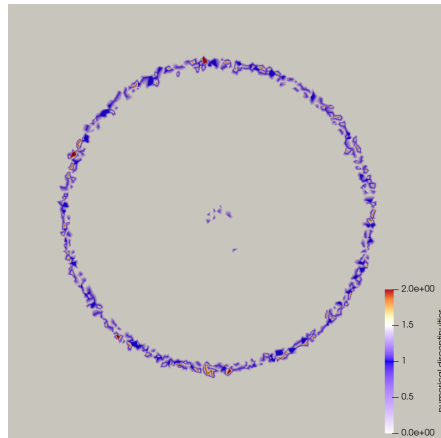
(a) f_5



(b) On a uniform grid of size 16,384.



(c) On the Delaunay triangulation of 16,384 randomly sampled points.



(d) On the Delaunay triangulation of 65,536 randomly sampled points.

Figure 5: Function f_5 and C_1 discontinuities detected by RDI on three different meshes.

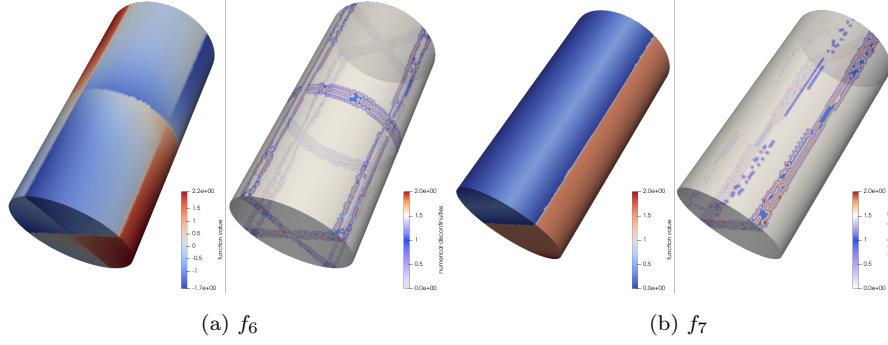


Figure 6: Function value and numerical discontinuities detected by RDI without virtual splitting on the surface triangulations of a cylinder.

respectively, where

$$g(x) = \begin{cases} x, & \text{if } 0 \leq x < \frac{1}{4}, \\ \frac{1}{2} - x, & \text{if } \frac{1}{4} \leq x < \frac{1}{2}, \\ \frac{3}{4}, & \text{if } \frac{1}{2} \leq x < \frac{3}{4}, \\ 16(x - \frac{3}{4})^3 + \frac{3}{4}, & \text{if } \frac{3}{4} \leq x \leq 1. \end{cases}$$

Figures 6 and 7 display the detected discontinuities on a cylinder and a reamer, respectively. It can be observed that RDI accurately detected the C^0 discontinuities. However, it missed part of the C^1 discontinuities as the quadratic WLS had minimal overshoots and undershoots for the given mesh resolution in the corresponding regions. Decreasing the threshold κ would make RDI more sensitive and miss fewer C^1 discontinuities, although it may also introduce some false positives.

5.4. Application to remap

Robust detection of discontinuities has a variety of applications. In this section, we demonstrate the use of RDI in remapping data between different meshes, also known as data remap. In this context, upon identifying C^0 and C^1 discontinuities, one can employ numerical techniques, such as WLS-ENO remap [13] and CAAS [37], to resolve the Gibbs phenomena [38]. Figure 8 compares

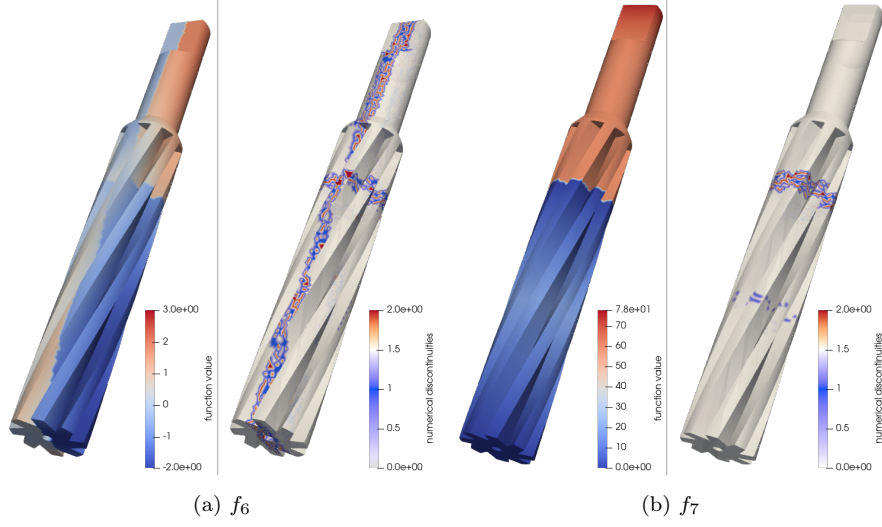


Figure 7: Function value and numerical discontinuities detected by RDI with virtual splitting on the surface triangulation of a reamer.

the remapping of f_2 using WLS and WLS-ENO on a sphere, where the former does not distinguish smooth and discontinuous regions and the latter adjusts the weighting schemes at discontinuities. As can be seen, the WLS result suffers from oscillations near discontinuities. In contrast, the combination of WLS-ENO and RDI successfully eliminated overshoots and undershoots while preserving accuracy in smooth regions.

6. Conclusions

In this paper, we have introduced the Robust Discontinuity Indicators (RDI) method, an innovative approach for the robust and efficient detection of discontinuities in the approximation of piecewise continuous functions over meshes. Our experiments and analyses have demonstrated the potential of the RDI in identifying both C^0 and C^1 discontinuities in node-based values and in addressing the challenges associated with non-uniform meshes and complex surface geometries.

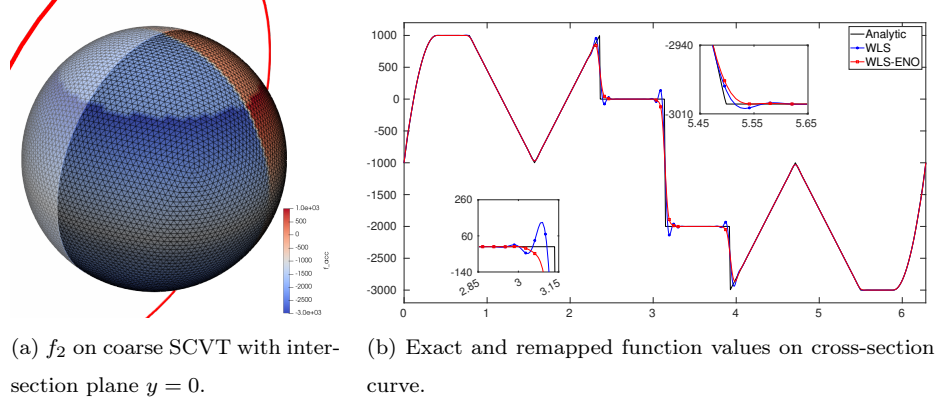


Figure 8: Comparison between original WLS and WLS-ENO without and with detection and treatment of discontinuities, respectively.

Despite the promising results obtained, several avenues exist for the further improvement and expansion of the RDI method. One potential enhancement involves incorporating a thinning process to refine the detected discontinuities further, thereby making them more precise. The implementation of this thinning process could significantly improve the fidelity of the approximation and further reduce the occurrence of the Gibbs phenomena, thereby enhancing the overall quality of the computational solution. Moreover, the present work primarily focused on 2D surfaces, creating an opportunity for the extension of the RDI method to three dimensions. Such an extension would significantly broaden the application range of the RDI method, allowing it to accommodate more complex real-world scenarios found in fields such as fluid dynamics, material science, and medical imaging.

In conclusion, the RDI method represents a significant step forward in the robust and efficient detection of discontinuities in piecewise continuous function approximations. The potential improvements and expansions identified will pave the way for further research and development in this critical area, with the ultimate goal of achieving more accurate and efficient computational methods.

Acknowledgments

This work was supported under the Scientific Discovery through Advanced Computing (SciDAC) program in the US Department of Energy’s Office of Science, Office of Advanced Scientific Computing Research through subcontract #462974 with Los Alamos National Laboratory.

References

- [1] J. S. Hesthaven, T. Warburton, Nodal Discontinuous Galerkin Methods, Springer, 2008.
- [2] M. Botsch, L. Kobbelt, M. Pauly, P. Alliez, B. Lévy, Polygon Mesh Processing, CRC Press, 2010.
- [3] R. J. LeVeque, Finite Volume Methods for Hyperbolic Problems, Cambridge University Press, 2002.
- [4] D. Gottlieb, C. W. Shu, On the Gibbs phenomenon and its resolution, SIAM Rev. 39 (4) (1997) 644–668.
- [5] X.-D. Liu, S. Osher, T. Chan, Weighted essentially non-oscillatory schemes, J. Comput. Phys. 115 (1) (1994) 200–212.
- [6] Y. Li, Q. Chen, X. Wang, X. Jiao, WLS-ENO remap: Superconvergent and non-oscillatory weighted least squares data transfer on surfaces, J. Comput. Phys. 417 (2020) 109578.
- [7] E. Tadmor, Filters, mollifiers and the computation of the Gibbs phenomenon, Acta Numer. 16 (2007) 305–378.
- [8] D. Cates, A. Gelb, Detecting derivative discontinuity locations in piecewise continuous functions from Fourier spectral data, Numer. Algo. 46 (1) (2007) 59–84.
- [9] E. Hewitt, R. E. Hewitt, The Gibbs-Wilbraham phenomenon: an episode in Fourier analysis, Arch. Hist. Exact Sci. 21 (2) (1979) 129–160.

- [10] M. Bozzini, M. Rossini, The detection and recovery of discontinuity curves from scattered data, *J. Comput. Appl. Math.* 240 (2013) 148–162.
- [11] M. C. L. de Silanes, M. C. Parra, J. J. Torrens, Vertical and oblique fault detection in explicit surfaces, *J. Comput. Appl. Math.* 140 (1-2) (2002) 559–585.
- [12] R. C. Moura, A. Cassinelli, A. F. da Silva, E. Burman, S. J. Sherwin, Gradient jump penalty stabilisation of spectral/hp element discretisation for under-resolved turbulence simulations, *Comput. Methods Appl. Mech. Eng.* 388 (2022) 114200.
- [13] Y. Li, X. Zhao, N. Ray, X. Jiao, Compact feature-aware Hermite-style high-order surface reconstruction, *Engrg. Comput.* (2019) 1–24.
- [14] G. T. Shrivakshan, A comparison of various edge detection techniques used in image processing, *Int. J. Comput. Sci. Issues* 9 (5) (2012) 269.
- [15] R. Archibald, A. Gelb, J. Yoon, Polynomial fitting for edge detection in irregularly sampled signals and images, *SIAM J. Numer. Ana.* 43 (1) (2005) 259–279.
- [16] R. Saxena, A. Gelb, H. Mittelmann, A high order method for determining the edges in the gradient of a function, *Comm. Comput. Phys.* 5 (2-4) (2009) 694–711.
- [17] R. Archibald, A. Gelb, J. Yoon, Determining the locations and discontinuities in the derivatives of functions, *Appl. Numer. Math.* 58 (5) (2008) 577–592.
- [18] D. Marr, E. Hildreth, Theory of edge detection, *Proc. Roy. Soc. London* 207 (1167) (1980) 187–217.
- [19] D. Marr, Early processing of visual information, *Philos. Trans. R. Soc. Lond. B Biol. Sci.* 275 (942) (1976) 483–519.

- [20] D. Marr, S. Ullman, T. Poggio, Bandpass channels, zero-crossings, and early visual information processing, *J. Opt. Soc. Am.* 69 (6) (1979) 914–916.
- [21] S. Mallat, W. L. Hwang, Singularity detection and processing with wavelets, *IEEE Trans. Inf. Theory* 38 (2) (1992) 617–643.
- [22] X. Jiao, H. Zha, Consistent computation of first- and second-order differential quantities for surface meshes, in: *ACM Solid and Physical Modeling Symposium*, ACM, 2008, pp. 159–170.
- [23] M. D. Buhmann, *Radial Basis Functions: Theory and Implementations*, Vol. 12, Cambridge University Press, 2003.
- [24] C. Hu, C.-W. Shu, Weighted essentially non-oscillatory schemes on triangular meshes, *J. Comput. Phys.* 150 (1) (1999) 97–127.
- [25] J. Shi, C. Hu, C.-W. Shu, A technique of treating negative weights in WENO schemes, *J. Comput. Phys.* 175 (1) (2002) 108–127.
- [26] Z. Xu, Y. Liu, H. Du, G. Lin, C.-W. Shu, Point-wise hierarchical reconstruction for discontinuous Galerkin and finite volume methods for solving conservation laws, *J. Comput. Phys.* 230 (17) (2011) 6843–6865.
- [27] Y.-T. Zhang, C.-W. Shu, Third order WENO scheme on three dimensional tetrahedral meshes, *Comm. Comput. Phys.* 5 (2-4) (2009) 836–848.
- [28] Y. Liu, Y.-T. Zhang, A robust reconstruction for unstructured WENO schemes, *J. Sci. Comput.* 54 (2,3) (2013) 603–621.
- [29] X. Jiao, D. Wang, Reconstructing high-order surfaces for meshing, *Engrg. Comput.* 28 (2012) 361–373.
- [30] M. Buhmann, A new class of radial basis functions with compact support, *Math. Comput.* 70 (233) (2001) 307–318.

- [31] N. Ray, D. Wang, X. Jiao, J. Glimm, High-order numerical integration over discrete surfaces, *SIAM J. Numer. Ana.* 50 (2012) 3061–3083.
- [32] V. Dyedov, N. Ray, D. Einstein, X. Jiao, T. Tautges, AHF: Array-based half-facet data structure for mixed-dimensional and non-manifold meshes, in: J. Sarrate, M. Staten (Eds.), *Proceedings of the 22nd International Meshing Roundtable*, Springer International Publishing, 2014, pp. 445–464.
- [33] J. Humpherys, T. J. Jarvis, E. J. Evans, *Foundations of Applied Mathematics, Volume I: Mathematical Analysis*, SIAM, 2017.
- [34] L. Ju, T. Ringler, M. Gunzburger, Voronoi tessellations and their application to climate and global modeling, in: *Numerical Techniques for Global Atmospheric Models*, Springer, 2011, pp. 313–342.
- [35] R. J. LeVeque, *Numerical Methods for Conservation Laws*, Vol. 132, Springer, 1992.
- [36] L. A. Shepp, B. F. Logan, The Fourier reconstruction of a head section, *IEEE Trans. Nucl. Sci.* 21 (3) (1974) 21–43.
- [37] A. M. Bradley, P. A. Bosler, O. Guba, M. A. Taylor, G. A. Barnett, Communication-efficient property preservation in tracer transport, *SIAM J. Sci. Comput.* 41 (3) (2019) C161–C193.
- [38] D. Gottlieb, C.-W. Shu, On the Gibbs phenomenon and its resolution, *SIAM Rev.* 39 (4) (1997) 644–668.

Appendix A. The Effect of Virtual Splitting along Sharp Features

A general surface might have geometric discontinuities, such as features and ridge points. Running RDI on such geometric discontinuities directly might yield inaccurate detection of numerical discontinuities. Specifically, a smooth function in the Euclidean space could often be misclassified as C^1 discontinuity near the geometric feature and ridge points. Conversely, a function with C^1

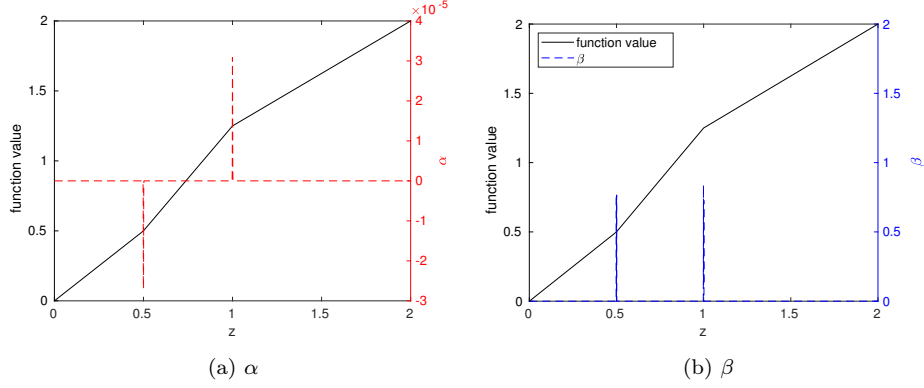


Figure A.9: α and β values of f_6 on Γ . The black line is the function value of f_6 . In (a), the red dash line is α . In (b), the blue dash line is β .

discontinuity that coincide with the geometric discontinuity might be mistaken as a smooth function.

To illustrate these two cases, let us first consider two functions $f_6(x, y, z) = g_1(x, y, z, 0.5)$ and $f_7(x, y, z) = g_1(x, y, z, 1)$ on a curve $\Gamma = \{(t, g_2(t), t) | t \in \mathbb{R}\}$, where

$$g_1(x, y, z, a) = \begin{cases} a + \frac{3}{2}(y - a), & z > a, \\ x, & z \leq a, \end{cases}$$

and

$$g_2(t) = \begin{cases} 1 + \frac{1}{2}(t - 1), & t > 1, \\ t, & t \leq 1, \end{cases}$$

are two piecewise smooth functions. $g_1(x, y, z, a)$ has a C^1 discontinuity at $z = a$ on Γ if $a \leq 1$, since the gradients are $(0, \frac{3}{2}, 0)$ and $(0, 0, 1)$ on two sides of $z = a$. However, using RDI directly without virtual splitting would result in false positives for f_6 and false negatives for f_7 , respectively.

Figure A.9 shows that RDI without virtual splitting can detect the C^1 discontinuity at $z = a = 0.5$. However, it also erroneously classified the smooth region near $z = 1$ as C^1 discontinuity. Figure A.10 illustrates that RDI without virtual splitting could miss the C^1 discontinuity at $z = a = 1$ because $\beta \equiv 0$.

Similar misclassifications can also occur on surface meshes without virtual

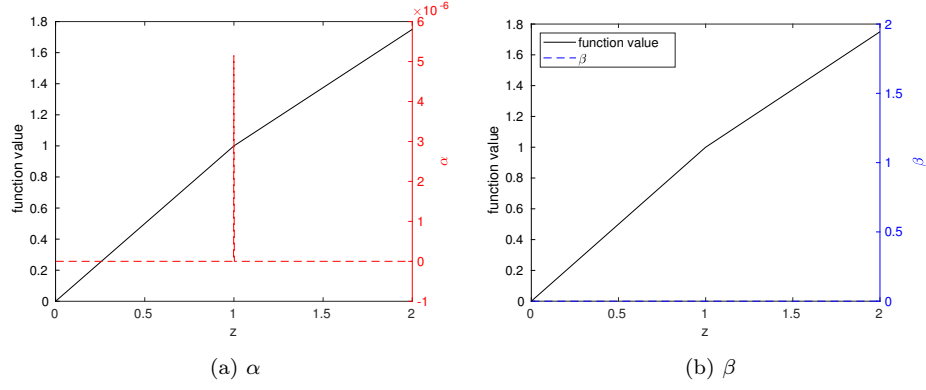


Figure A.10: α and β of f_7 on Γ . The black line is the function value of f_7 . In (a), the red dash line is α . In (b), the blue dash line is β .

splitting. For instance, Figure A.11 illustrates that RDI without virtual splitting on the triangulation of a cylinder for a simple smooth function $f_6(x, y, z) = z + 2$. The smooth function f_6 in the Euclidean space is constant on the two bases and linear on the lateral surface. RDI with virtual splitting produced expected results. In contrast, RDI without virtual splitting would yield false positives near the features on the bases.

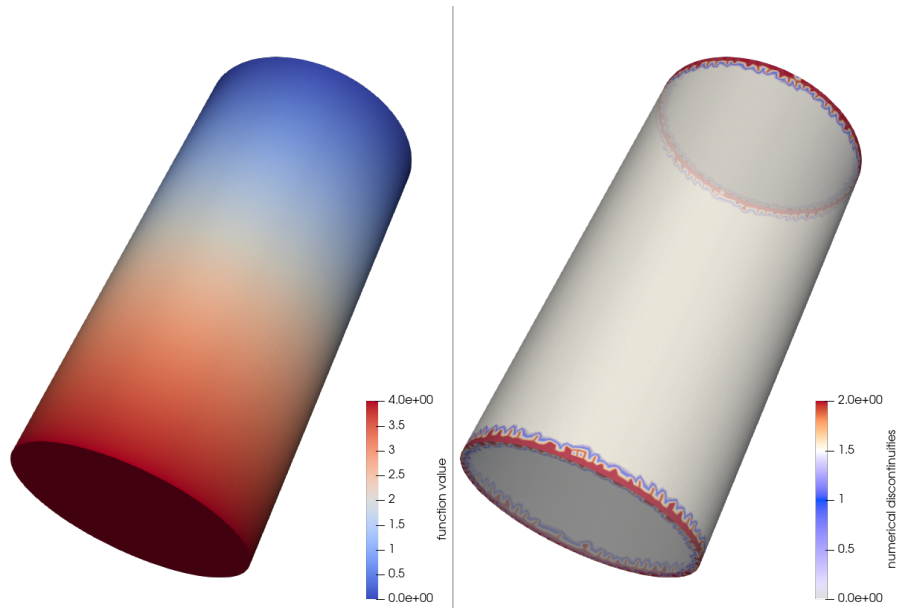


Figure A.11: Function value (left) and numerical discontinuities detected by RDI without virtual splitting (right) of f_6 on the triangulation of a cylinder.